Nano Energy 103 (2022) 107843

Contents lists available at ScienceDirect

Nano Energy

journal homepage: www.elsevier.com/locate/nanoen

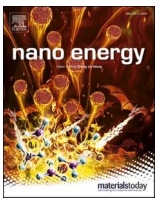

Catalysis of nickel nanodomains on Li-F dissociation for high-capacity fluoride cathodes with prior delithiation ability

Tao Wu [a], Yanhua Cui [a,**], Kaiyuan Wei [a], Chuanzhong Lai [b,c,d], Yu Zhao [e], Shuang Ni [e], Yongjin Chen [f], Xiang Gao [f], Yixiu Cui [a], Chilin Li [b,c,d,*]

[a] Laboratory of Electrochemical Power Sources, Institute of Electronic Engineering, China Academy of Engineering Physics, Mianyang, Sichuan 621000, China
[b] CAS Key Laboratory of Materials for Energy Conversion, Shanghai Institute of Ceramics, Chinese Academy of Sciences, Shanghai 201899, China
[c] Center of Materials Science and Optoelectronics Engineering, University of Chinese Academy of Sciences, Beijing 100049, China
[d] State Key Laboratory of High Performance Ceramics and Superfine Microstructure, Shanghai Institute of Ceramics, Chinese Academy of Sciences, 585 He Shuo Road, Shanghai 201899, China
[e] Reaserch Center of Laser Fusion, China Academy of Engineering Physics, Mianyang, Sichuan 621000, China
[f] Center for High Pressure Science and Technology Advanced Research (HPSTAR), Building 8, No.10 Xibeiwang East Rd., Beijing 100094, China

ARTICLE INFO

Keywords:
LiF splitting
Conversion reaction
Catalysis effect
Ternary fluoride cathode
High-capacity Li batteries

ABSTRACT

Transition metal fluoride is being considered as one of the most promising cathode materials due to its feasibility of high-voltage conversion reaction and high theoretical capacity. But the low solubility of LiF in fluoride is prone to degrade the electrode conductivity and Li-resource supply from fluoride cathode side, therefore limiting the reversibility of conversion reaction and its practical use in Li-ion batteries. Here, we propose a catalysis effect of Ni nanodomains to activate the Li-F splitting with much lower dissociation energy and to enable the LiF/Fe/Ni ternary cathode with superior conversion reaction capacity (600 mAh g^{-1}) and rate performance (306 mAh g^{-1} at 3.8 A g^{-1}). The crowded effect between LiF and dual-metal phases suppresses the growth of crystal grains and promotes the enrichment and penetration of LiF-Fe-Ni triple-phase interfaces. This compact interface contact endows the lithiated fluoride with an ultrahigh initial charge capacity exceeding 600 mAh g^{-1} and lowered charge plateau below 3.5 V. The preservation of interconnectivity and catalytic activity of electron conductive network enables the high reversibility of LiF splitting/recombination under high energy efficiency of 76%, as well as the electrochemical synthesis of rutile-like $Ni_xFe_{1-x}F_2$ solid-solution phase. This fluoride cathode enables a release of high energy density (1414 Wh kg^{-1}) under a power density of 849 W kg^{-1} and the energy density can still be preserved at 629 Wh kg^{-1} under an extremely high power densities of 3374 W kg^{-1}. This work paves the way to develop the high-energy-density fluoride cathodes with the prior delithiation ability, which can lessen and even eliminate the use of Li metal at anode side.

1. Introduction

Lithium-ion batteries have become the most widely used battery system in view of the broad applications from microchips to electric vehicles [1]. However, the traditional cathode materials (e.g. $LiCoO_2$, $LiFePO_4$ and their derivatives) based on Li insertion/extraction reactions are inherently confined by their single-electron redox mechanism, which cannot meet the high-capacity and high-energy-density demands for commercial applications [2]. Otherwise, conversion-type cathode materials, especially transition metal fluorides, have raised considerable attention in order to meet the future energy storage requirement due to their lower costs (e.g. by using Fe element), higher capacities (> 500 mAh/g) and improved safety characteristics (e.g. by suppressing O_2 gas evolution) compared to the traditional intercalation-type cathodes [3–5]. The metal fluorides (MF_x) can accommodate multiple Li^+ through both the intercalation and conversion reactions, generating metal (M) and LiF upon discharge based on the equation: $MF_x + xLi^+ + xe^- \rightarrow xLiF + M$ [6,7]. However the reconversion process involving the electrochemical splitting of insulating LiF is still a big challenge.

* Corresponding author at: CAS Key Laboratory of Materials for Energy Conversion, Shanghai Institute of Ceramics, Chinese Academy of Sciences, Shanghai 201899, China.
** Corresponding author.
E-mail addresses: cuiyanhua@netease.com (Y. Cui), chilinli@mail.sic.ac.cn (C. Li).

https://doi.org/10.1016/j.nanoen.2022.107843
Received 20 May 2022; Received in revised form 12 September 2022; Accepted 20 September 2022
Available online 22 September 2022

In addition, the development of transition metal fluorides is also prevented by other multiple challenges. One of the barriers for conversion fluoride cathodes is the volume change along with the cation and F^- dissolutions into electrolyte during conversion reaction [8–11]. This factor brings about the electric contact degradation and mass loss of active species. Another serious limitation for ionic bonding dominated fluorides is the intrinsically poor electronic conductivity, resulting in the facile formation and accumulation of passivated reaction zones or dead reaction products [12,13]. It is prone to lead to the large voltage hysteresis between charge and discharge curves as well as capacity fading as observed in many conversion cathodes [14,15]. In order to improve the cathode conductivity and confinement effect, high-energy ball milling method and solution modulation synthesis with the electron wiring of highly conductive additive (e.g. carbon black and carbon nanotube) had been widely used [16–18]. These mechanical and chemical methods also enable the reduction of fluoride particle size, leading to the dual shortening of ion and electron diffusion distances [16,19]. Wang et al. found that the electrochemical conversion of FeF_2 actually enables the formation and penetration of internal wiring network consisting of interconnected metallic Fe nanodomains with a size less than 5 nm in diameter, which could provide the continuous electron transport pathway inside individual particle and electron linkage to the external conductive work. These metallic nanodomains also enable the sufficient contact with surrounding LiF matrix and promote its splitting during recharging. This optimized Fe/LiF distribution guarantees the reversibility of conversion reaction [20]. The introduction of hetero-metallic cation with potentially higher reduction potential can help with the lowering of cycling hysteresis as demonstrated in the solid-solution $Cu_yFe_{1-y}F_2$ [17]. The nanocomposite $Cu_{0.5}Fe_{0.5}F_2$ delivered a small hysteresis less than 150 mV with a high capacity of 543 mAh g^{-1}, indicating that cation substitution is an effective avenue for tailoring the key electrochemical properties of conversion-type fluorides. However not all the theoretically high-voltage cations or their combination can contribute to the narrowing of cycling hysteresis as indicated in the cases of $Ni_xCo_{1-x}F_2$ and $Ni_yFe_{1-y}F_2$ [21,22]. Their discharge voltages are even below 1.5 and 2 V respectively. The spontaneous degradation of inner conductive pathway during cycling should is responsible for the low voltage output. Therefore the prior optimization of heterogeneous interfaces and conductive network is crucial to achieve high-performance fluoride cathodes.

On the other hand, the conversion-type fluorides are usually Li-free at the pristine state. However in order to decrease the amount of Li metal at the anode side and even to utilize the Li-free anode system, the pre-lithiation of fluoride is highly required. In contrast to oxide cathodes with high Li solubility, the pre-lithiation on fluorides with low Li solubility would cause the precipitation of LiF insulating phase. Previous reports have demonstrated that the conversion of LiF during the first charge process is quite sluggish, leading to large voltage polarization and low energy efficiency [23,24]. The sluggish LiF splitting results in the insufficient capacity release and accumulation of unreactive LiF even under the protocol of high cut-off voltage. This low-efficiency charging would also accelerate the electrolyte decomposition and degrade the following cycling. The high-energy ball milling of LiF and transition metal oxide MO (e.g. MnO, FeO, CoO) or fluoride MF_2 (e.g. FeF_2) with low valence state of M cation was reported to enable the lowering of charge voltage [25,26]. However most of the charge capacity is still released above 4 V and it is limited due to the single-electron reaction. The combination of LiF and metallic M is expected to enable the more electron transfer and theoretically higher charge capacity, but their lattice mismatch is prone to degrade or loosen the reaction interfaces [27]. Therefore some unstable pre-lithiation agents (e.g. LiH, Li_3N) were introduced in FeF_x systems to trigger the spontaneous conversion reaction with the formation of intimate and active LiF/M interfaces, which are expected to take the similar effect as in the case of electrochemical lithiation of FeF_x [24,28]. However the practical capacity release is still insufficient and most of the discharge capacity is below 2 V, leading to low energy efficiency. These results indicate the limitation of powder fluoride systems in terms of the difficult optimization of conductive network and the lacking of crowded effect of multiphase domains. Therefore the tailoring of grain morphology and introduction of doping component did not always bring about the desired performance improvement [23,29].

To address the issue of LiF splitting, recently we developed a combinatorial co-deposition method to construct the compact LiF/metal and LiF/oxide heterogeneous interfaces between tiny nanodomains [30,31]. This method enriches the choice of reactive and catalytic components, which remarkably improve the LiF splitting kinetics and energy efficiency of cycling. For instance, for the composites of LiF/Fe-Cu and LiF-$NiFe_2O_4$, the initial charge process was smoothly achieved under a cut-off voltage of 4 V with a considerable capacity release of 200–300 mAh g^{-1}. The resultant energy efficiency was as high as 88%. However the reversible capacities in these systems were still smaller than 400 mAh g^{-1}, far from the theoretical capacity. Therefore it is highly desired to explore the more advanced heterostructure for more sufficient LiF splitting and capacity release. Here, we propose the synergic catalysis of Fe and Ni nanodomains with compact conductive network to activate the LiF splitting in the LiF/Fe/Ni ternary thin film system prepared by pulse laser deposition (PLD). The crowded effect of multiphases suppresses the growth of crystal grains and promotes the enrichment and penetration of LiF-metal interfaces. The existence of triple phase interface endows the LiF/Fe/Ni cathode (denoted as NFF with Ni: Fe: LiF = 1:1:4 in molar ratio) with much longer charge plateau below 3.5 V and much larger charge capacity exceeding 600 mAh g^{-1} during the first charge process. The following capacity is as high as 600 mAh g^{-1} and still preserved at 500 mAh g^{-1} after 10 cycles. The density functional theory (DFT) calculations disclose the catalysis effect of Ni nanodomains on lowering the dissociation energy of LiF and activating the conversion reaction kinetics. The blending of Ni into LiF/Fe system promotes the electrochemical synthesis of rutile-like $Ni_xFe_{1-x}F_2$ solid-solution phase and improvement of energy efficiency (76%).

2. Results and discussion

Fig. 1a shows the X-ray diffraction (XRD) patterns of the composite target of LiF/Ni/Fe (with a molar ratio of 4:1:1), as prepared NFF thin film, as well as film electrodes after charge to 4 V and discharge to 1.5 V. The diffraction pattern of composite target belongs to the mixture of crystalline LiF (JCPDS No. 45–1460), Ni (JCPDS No. 04–0850) and Fe (JCPDS No. 06–0696) [32]. The strong diffraction peaks at 40.1°, 46.5° and 67.8° are attributed to Pt_3Ti phase (JCPDS No.17 −0064), which is formed by the thermal alloying of Ti and Pt thin films (as current collector) pre-deposited on the Si substrate [33]. The diffraction peaks of NFF thin film are broad and can be found mainly at 38.7°, 43.3°, 44.7°, 45.0° and 65.5°, corresponding to the LiF (111), Ni (111), Fe (110), LiF (200) and LiF (220) planes respectively [34], indicating the nanocrystalline structure of NFF with suppressed crystal grain growth. Note that after the first charge to 4 V, these peaks are remarkably attenuated, confirming the electrochemical splitting of LiF along with the oxidation (or fluorination) of metallic Ni and Fe. After the following discharge to 1.5 V, the re-emerging peaks are consistent with the pristine sample, demonstrating the excellent reversibility of conversion reaction [35]. The high-resolution transmission electron microscope (HRTEM) image and the selected area electron diffraction (SAED) pattern are shown in Figs. 1b and 1c to disclose the interface of triple phase contact between LiF, Ni and Fe nanodomains. The SAED pattern composed of concentric rings shows the polycrystalline structure, which is consistent with the XRD result. Scanning electron microscope (SEM) images display the surface and cross-section morphologies of NFF thin film in Fig. 1d and e respectively. This NFF film is dense and roughly smooth with a thickness of 158 nm. Its grains are compactly stacked with narrow grain boundaries, which can still provide enough channels for facile electrolyte penetration [36]. From the scanning transmission electron microscopy

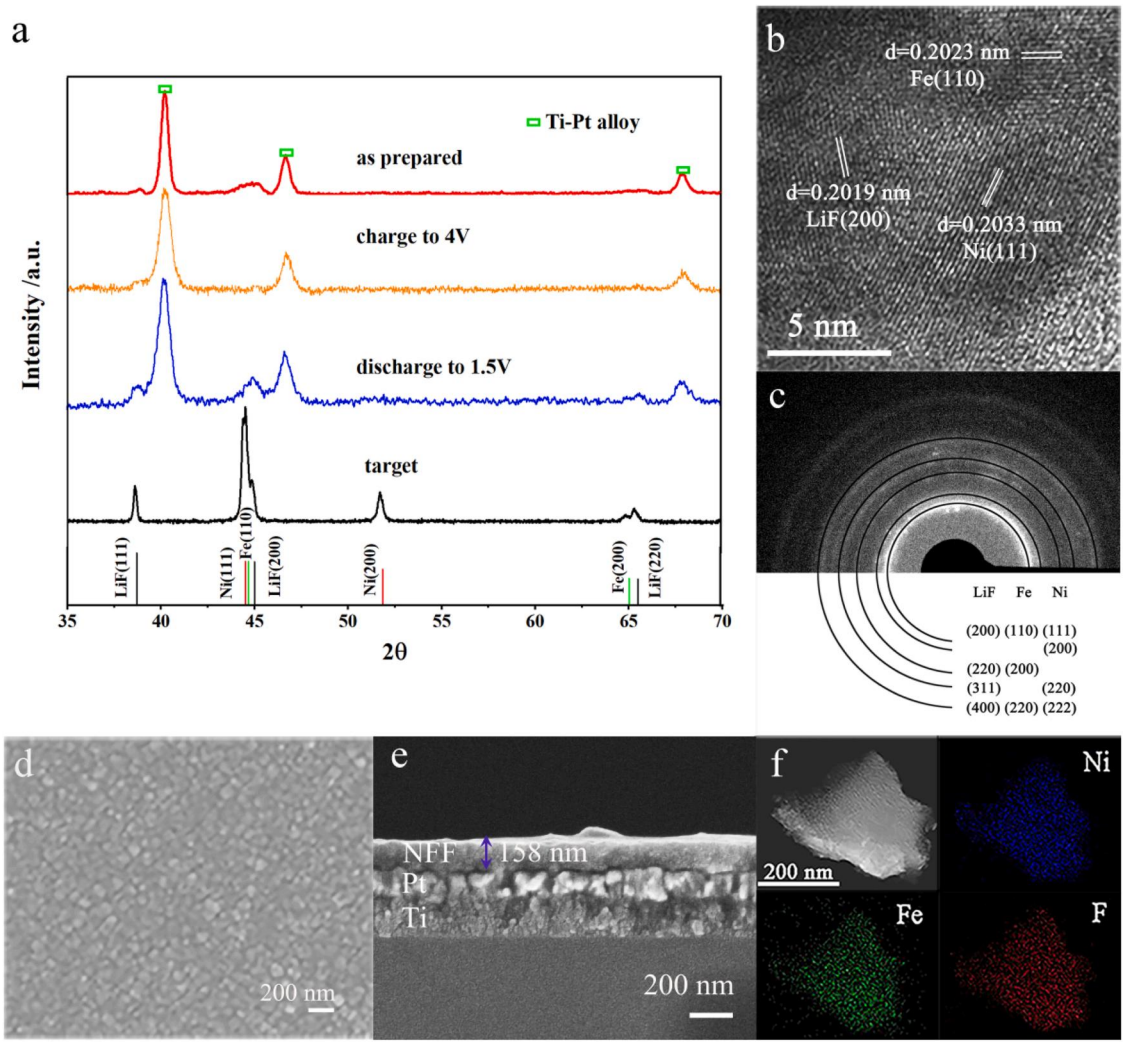

Fig. 1. (a) XRD patterns of Ni/Fe/LiF target in a molar ratio of 1:1:4, pristine and cycled NFF thin films after charge to 4 V and discharge to 1.5 V. (b) HRTEM image and (c) corresponding SAED pattern of NFF thin film. (d) Surface and (e) cross-section SEM images of NFF thin film. (f) STEM elemental mapping images of Ni, Fe and F.

with energy dispersive spectrum (STEM-EDS) as shown in Fig. 1f, the uniform coloring of related elements (Ni, Fe and F) further confirms the sufficient contact of LiF, Ni and Fe domains with homogeneous spatial distribution. The atomic ratio of Ni, Fe and F in NFF thin film is estimated based on EDS counts, and it is almost consistent with the pre-set mole ratio of Ni: Fe: LiF = 1:1:4 in the source target (Fig. S1).

The electrochemical performance of a series of NFF films with different Ni/Fe/LiF ratios were investigated systematically. The cyclic voltammetry (CV) curves and charge/discharge profiles based on different xNi/(1-x)Fe/2LiF (x = 0.1–0.9) ratios during the second cycle are shown in Fig. S2 and S3. One can note two modification tendencies from the CV evolution when the x value is close to 0.5. One is the overall intensification of current response, and the other is the fraction increase of the anodic peak (at 2.95 V) with smaller overpotential compared with the anodic peak at 3.3 V. These tendencies indicate the promotion effect of conversion reaction kinetics by the comparable contents of metallic Fe and Ni nanodomains. The electromotive force (EMF) of NiF_2 is 2.964 V, which is higher than both the EMF values of FeF_3 and FeF_2 (2.742 and 2.664 V respectively) [37]. However, as observed from the CV evolution, the increase of Ni content does not always cause the fraction increase of higher-voltage anodic peak (around 3.3 V) especially when its x value does not exceed 0.5. This phenomenon indicates a synergic catalysis effect of dual metal domains on lowering the charge overpotential. In the cases of asymmetric contents with x = 0.1 and 0.9, the Fe-dominant system displays the better electrochemical activity than the Ni-dominant one, in view of the potentially better distribution of built-in conductive network for the former [7,20]. The moderate introduction of Ni hetero-domains would not degrade this conductive network and on the contrary it provides the extra catalytic sites for LiF splitting. Therefore both the cathodic and anodic peaks become much more intensified in view of the higher utilization ratio of LiF conversion. Fig. S3 shows the corresponding charge/discharge profiles with the similar evolution tendency as the CV curves. The NFF sample based on the 0.5Ni/0.5Fe/2LiF ratio displays the highest reversible capacity (> 550 mAh g^{-1}) with two high discharge platforms (above 3 V and 2 V).

The CV curves based on different ratios of LiF are shown in Fig. 2a to check the influence of insufficient LiF amount. For the most optimized system of NFF cathode (Ni:Fe:LiF = 1:1:4), there are two pairs of typical oxidative and reductive peaks as observe at 3.3 V/3.1 V and 2.95 V/2.1 V (anodic/cathodic) respectively. The decrease of LiF fraction is not always favorable for the optimization of conductive network, although its overall electron conductivity should be improved. The extraction of LiF domains likely accelerates the growth and mergence of metallic domains into larger grains, which in turn degrade the interface contact with LiF nanodomains due to the size mismatch between LiF and metal grains. It would seriously dilute the triple-phase reaction/catalysis

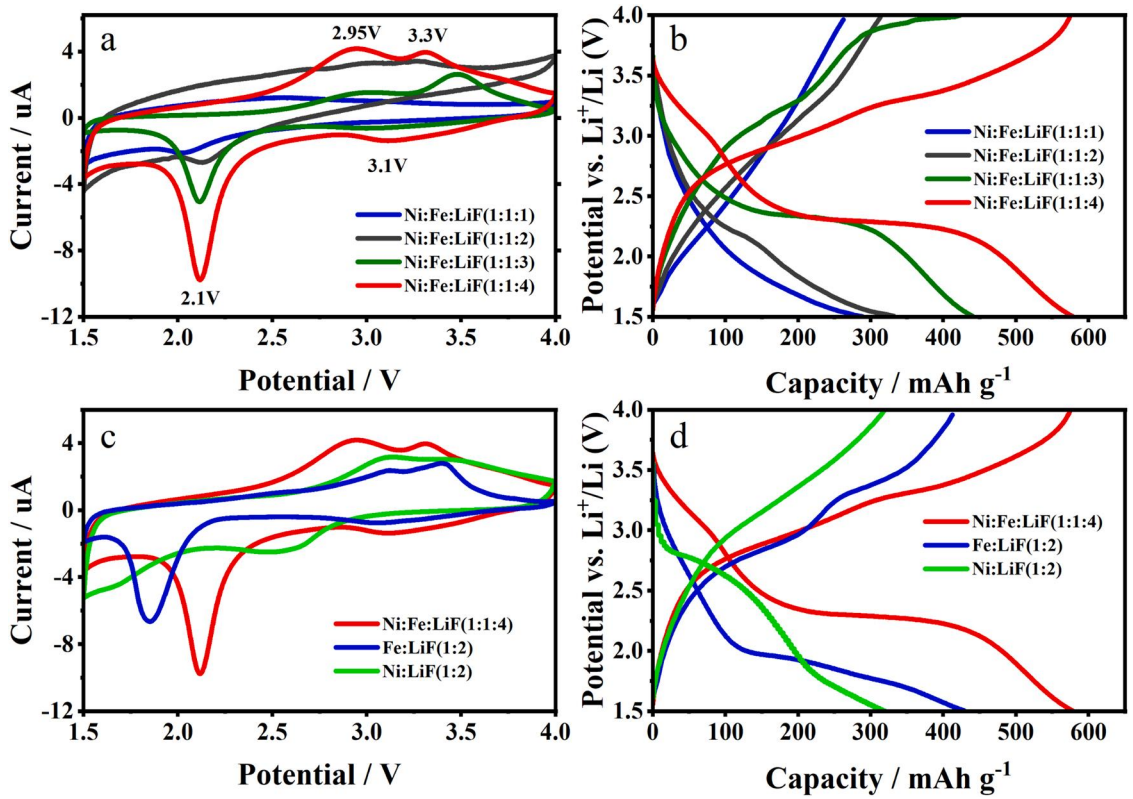

Fig. 2. (a) CV curves of Ni/Fe/xLiF (x = 1, 2, 3, 4) thin films at a scanning rate of 0.2 mV s^{-1}. (b) Charge/discharge curves of Ni/Fe/xLiF (x = 1, 2, 3, 4) thin films. (c) CV curves of ternary NFF, binary Ni/2LiF(1:2) and Fe/2LiF thin films at a scanning rate of 0.2 mV s^{-1}. (d) Charge/discharge curves of NFF, Ni/2LiF and Fe/2LiF thin films.

interfaces and therefore degrade the charge overpotential and capacity release as shown in the case of Ni:Fe:LiF = 1:1:3. The more extraction of LiF would even lead to the disappearance of distinct redox peaks (or discharge plateau) and leave a considerable amount of non-active metal grains as shown in the cases of Ni:Fe:LiF = 1:1:2 and 1:1:1. Fig. 2b displays the corresponding evolution of galvanostatic charge and discharge curves of NFF series. The optimized composition requires the sufficient supply of LiF in order to fully meet the Ni and Fe's redox power, and the fine dispersion of LiF domains would not influence the overall electron conductivity of electrode. As a consequence, the charge and discharge capacities can be close to 600 mAh g^{-1}, very close to the theoretical value of Ni/Fe/4LiF system (641 mAh g^{-1}). After the first charge activation, the following charge plateau voltage is evidently decreased, benefiting from the synergic catalysis of Ni-Fe domains on LiF splitting.

However, with the further increase of molar ratio of LiF to the formula of Ni/Fe/5LiF and Ni/Fe/6LiF, the excessive LiF would passivate the NFF cathode, leading to the inferior conversion kinetics with poorly-defined galvanostatic profiles and larger voltage polarization as shown in Fig. S4a and b [38]. Note that the reversible capacity of ternary composite Ni/Fe/4LiF is much higher than those of binary composite Ni/2LiF and Fe/2LiF cathodes (Fig. 2c and d). From both the CV and galvanostatic measurements, both the Fe and Ni based binary composites deliver the lower and higher discharge plateaus (below 2 V and above 2.5 V respectively). However in the Ni-Fe coexisting ternary composite, the discharge plateau profile is not a simple overlap of the profiles of binary composites, and rather lies in the voltage zone between 2 and 2.5 V with a longer and better defined plateau. Moreover a higher-voltage discharge plateau appears above 3 V with a capacity exceeding 100 mAh g^{-1}. These features further indicate the synergic effect of dual metallic domains, which enables the higher capacity release and energy efficiency during cycling. Therein the oxidation and reduction processes of Fe and Ni redox centers likely progress in a synchronous mode in the same voltage zone, instead of the asynchronous mode, although the Ni redox is prone to occur at higher voltage and the Fe redox at the lower voltage [37].

As known, among fluoride cathodes, Fe-based system enables the best electrochemical activity in view of the potential interconnectivity of built-in conductive networks consisting of Fe nanodomains. In this case, the introduction of Ni nanodomains into Fe/LiF system enables the further activation of LiF splitting and conversion reaction. This effect should be attributed to the catalysis function of Ni atoms on the dissociation process of LiF. We attempted to reveal this Ni-based catalysis through DFT calculations (Fig. 3). The dissociation energy of LiF, which decomposes into Li and F without the assistance of transition metal, was firstly calculated (as shown in Fig. S5), according to the expression as follows:

$$E = (E_{Li}+E_F) - E_{LiF}$$

where E_{Li}, E_F and E_{LiF} are the energies of isolated Li, F and LiF, respectively. These values are shown in Table S1 and the dissociation energy of LiF is estimated to be 6.35 eV (close to the result of Yang et al.) [39]. This value is highly high, leading to the difficult splitting of LiF in the common sense. However, under the catalysis of metallic Ni, the situation is greatly ameliorated. We selected the main Ni (111) plane to adsorb LiF and observe the evolution of dissociation energy, Li-F and Ni-F bond lengths. Before the calculation of dissociation energy of LiF on Ni(111), the most possible adsorption sites of LiF, Li and F on the metal surface should be checked. Three possible initial adsorption sites on Ni (111) are considered as indicated in Fig. S6 and S7 [40]. They are (1) the top site (the position on the top of a Ni atom), (2) the bridge site (the center of two neighboring Ni atoms in the outer layer), and (3) the hollow site (the center of three neighboring Ni atoms in the outer layer). The adsorption energy (E_{ad}) of Li, F or LiF on Ni surface can be expressed as follows:

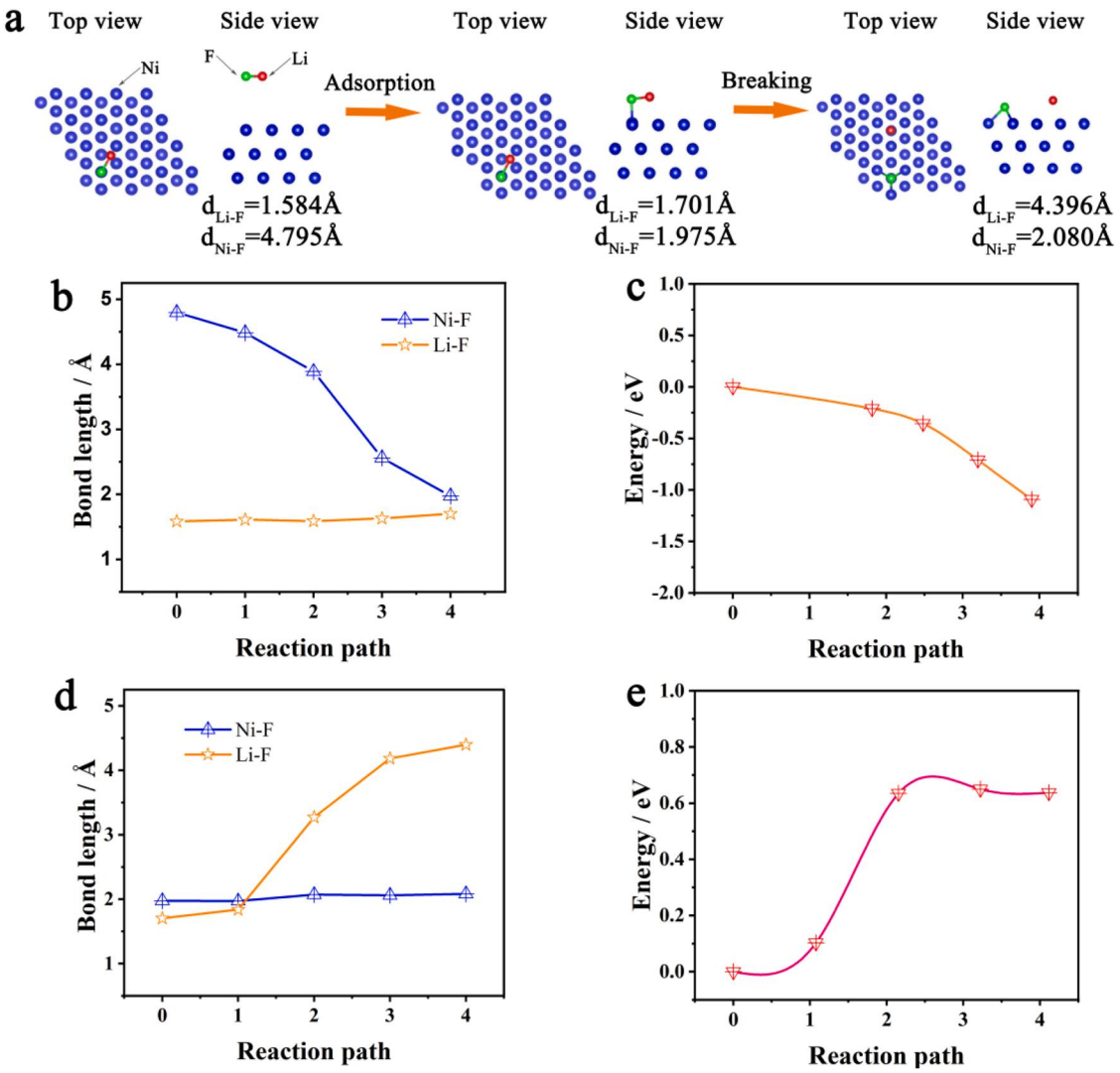

Fig. 3. (a) Schematic representation of adsorption and dissociation processes of LiF molecule on Ni (111) surface with the evolution of Li-F and Ni-F bond lengths. Evolution of (b) bond lengths and (c) corresponding adsorption energy barrier during the stabilization process of adsorption step by NEB method. Evolution of (d) bond lengths and (e) corresponding dissociation energy barrier of during the stabilization process of Li-F dissociation step by NEB method.

$$E_{ad} = -(E_{total} - E_{Ni} - E_{component})$$

where E_{total}, E_{Ni} and $E_{component}$ are the energies of total system, Ni (111) and isolated Li, F or LiF component, respectively. These values are shown in Table S2-S5. One can find that both the Li and F atoms on the bridge sites enable the highest adsorption energies of 2.585 eV and 4.164 eV, respectively. For the LiF configuration parallel to Ni (111), the bridge site also provides the highest adsorption energy (1.148 eV), and it is in accordance with the cases of single Li and F atoms.

After acquiring the preferential adsorption site, we then used the climbing image nudged elastic band (CI-NEB) method to compute the transition-state structures and corresponding dissociation energy barrier [41–43]. Based on the above optimization of LiF configuration on Ni surface, the adsorption of molecules on the bridge site is chosen as the initial structure. The potential reaction path is shown in Fig. 3 which contains the adsorption and dissociation processes. The Li-F bond length increases from 1.584 Å to 1.701 Å with the stabilization process of adsorption structure, while the Ni-F bond length decreases from 4.795 Å to 1.975 Å. During the dissociation process of LiF, the Li-F bond length is further increased to 4.396 Å with a dissociation energy barrier of LiF on Ni surface as small as 0.65 eV. This value is much smaller than that (6.35 eV) of LiF splitting without the pre-adsorption on metallic surface. This comparison indicates the remarkable catalysis of Ni domains on the decomposition of LiF.

Furthermore, the linear sweep voltammogram (LSV) curves were carried out to estimate the catalytic activity of various samples. As shown in Fig. 4a, b and c, the two oxidation peaks are ascribed to the reactions associated with LiF splitting and metal fluorination. Compared with the binary Ni/LiF and Fe/LiF electrodes, the ternary NFF electrode shows the best catalytic activity, which can be deduced from the largest peak area (Fig. 4a) and the steepest slope (Fig. 4b and c) [44,45]. Moreover, for NFF thin film its peak voltages shift to the lower values, also reflecting the optimization of catalytic activity and reconversion kinetics induced by dual metal nanodomains. In order to further disclose the charge transfer dynamics in NFF, Ni/LiF and Fe/LiF thin films, the corresponding cells were measured by Tafel analysis technique at the conversion reaction stage of discharge process (Fig. 4d) [46]. Therein the voltage was set at the respectively conversion platform for 1 h during the tenth discharge process, and then a linear sweep was performed at 1 mV s^{-1} with a voltage range of ± 150 mV around this selected open circuit voltage. The Tafel equation about the relationship between voltage polarization (η) and exchange current (i_0) is as follows [47]:

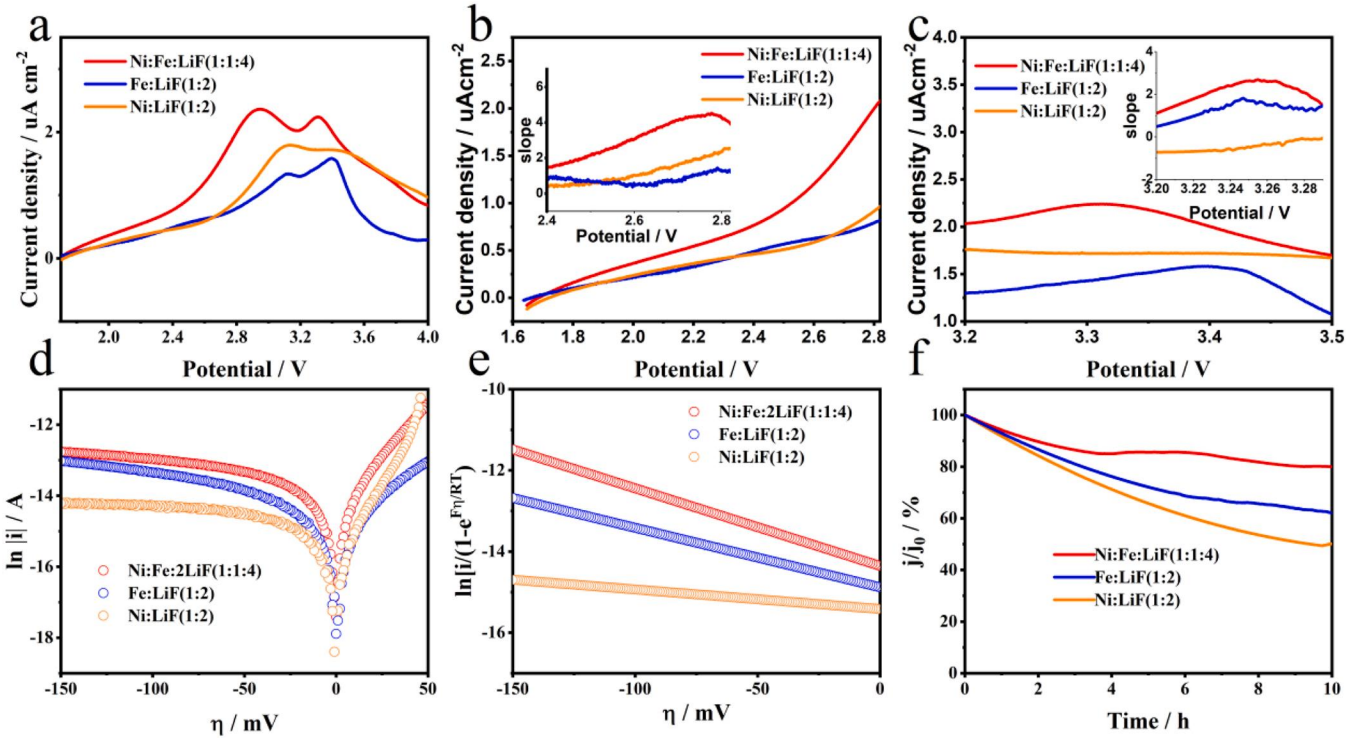

Fig. 4. (a) LSV curves of NFF films, Ni/2LiF and Fe/2LiF cathodes. Current responses of LSV curves around the anodic peaks (b) at the lower voltage region and (c) at the higher voltage region. Insets: corresponding slope curves. (d) Tafel plots of NFF films, Ni/2LiF and Fe/2LiF cathodes at the dominant conversion plateau region during lithiation process. (e) Corresponding Allen-Hickling plots with linear relationship to the intercept on vertical axis to determine the exchange current. (f) Chronoamperometric responses of NFF films, Fe/2LiF and Ni/2LiF cathodes.

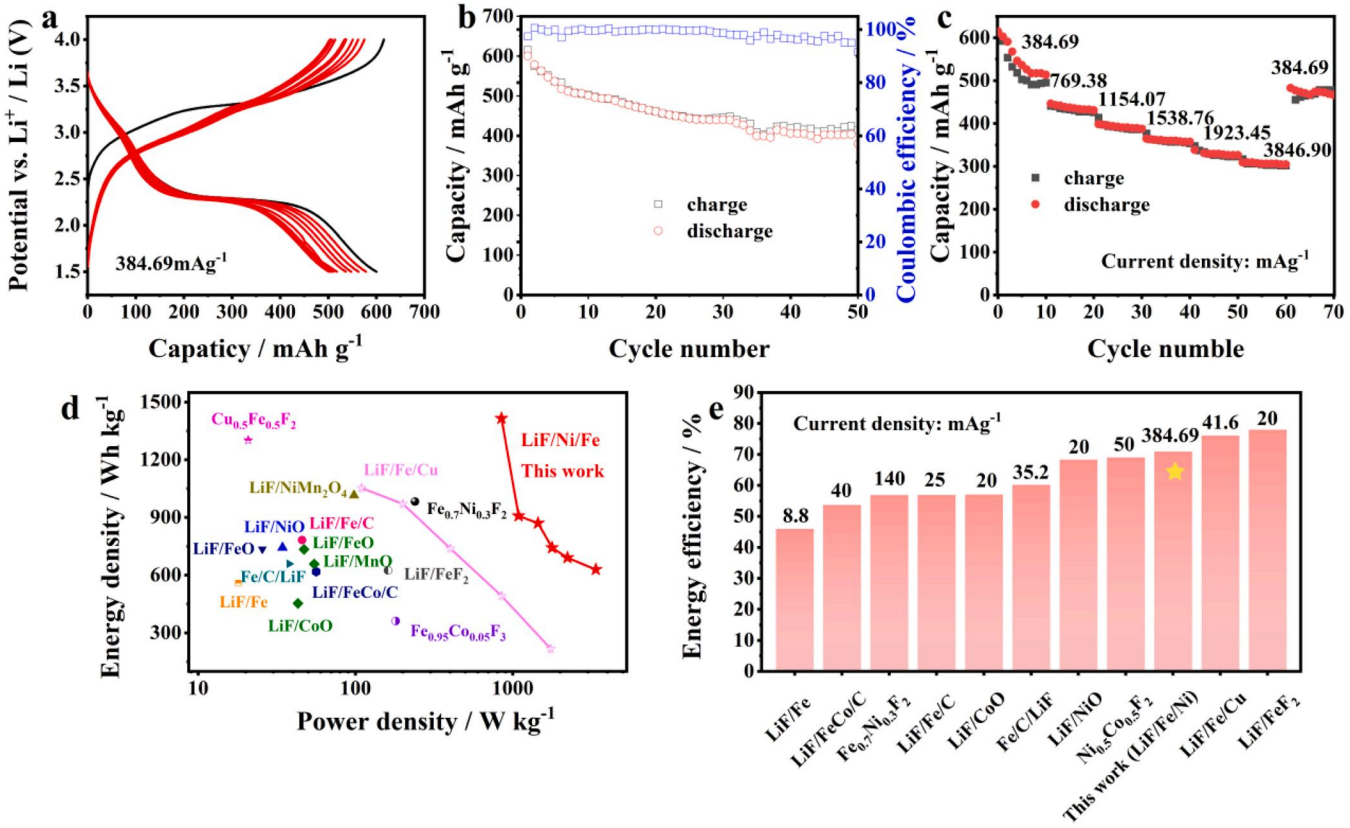

Fig. 5. (a) Galvanostatic charge-discharge curves of NFF cathode during the first 10 cycles in a potential range of 1.5–4.0 V. (b) Cycling performance and coulombic efficiency of NFF as a function of cycle number. (c) Rate capability of NFF thin film at high current densities. Comparison of (d) energy-power densities and (e) energy efficiency values between NFF and already reported LiF-driven conversion systems and ternary fluoride systems at the first cycle.

$$\eta = \frac{RT}{\alpha F}\ln i_0 - \frac{RT}{\alpha F}\ln i$$

where R, F, T, α and i are the gas constant, Faraday's constant, ambience temperature, charge transfer coefficient and current response, respectively. The Tafel result can be replotted according to the Allen-Hickling plots based on the Butler-Volmer equation as follows [48]:

$$\ln\left[\frac{i}{1-e^{\frac{F\eta}{RT}}}\right] = \ln i_0 - \frac{\alpha F}{RT}\eta$$

There is a linear relationship between the logarithmic current ($\ln i_0$) and voltage polarization (η) in the strong polarization region where the voltage is far enough from the equilibrium state. From the vertical axis intercept of the linear fitting of Allen-Hickling plots (Fig. 4e), the NFF thin film exhibits a evidently higher exchange current than the Ni/LiF and Fe/LiF thin films, further indicating the charge transfer advantage and better catalysis in ternary NFF system. Furthermore, the electrochemical kinetics of NFF electrode was also studied by the chronoamperometric test (Fig. 4 f). In response to a potential step perturbation, the faradaic current near the electrode surface decreases with the relaxation time due to the mass diffusion limitation. The smaller decrease degree of current response indicates the faster mass diffusion. The NFF thin film enables a preservation of about 80% of the initial current density even after continuous operation for 10 h, whereas the current densities of Ni/LiF and Fe/LiF decay to about 62% and 50% of their initial values. This comparison illustrates the superior kinetics of NFF thin film with sufficient faradaic reaction.

Fig. 5 shows the cyclic and rate performance of NFF thin film cathode. Note that the initial charge process to activate LiF splitting can achieve a charge capacity exceeding 600 mAh g^{-1}, which is record-high among the pre-lithiated fluoride cathodes and very close to the theoretical capacity (641 mAh g^{-1}). Moreover most of the charge capacity can be achieved below 3.5 V, leading to a high energy efficiency of 71% even at a high current density of 385 mA g^{-1}. This energy efficiency value is higher than most of the reported pre-lithiated fluorides and many Li-free fluorides even under the current densities one order of magnitude lower [21–28,30,49]. The following discharge capacity is still as high as 600 mAh g^{-1} and still preserved at 500 mAh g^{-1} after 10 cycles. The following voltage profiles are highly duplicated, benefiting from the high path reversibility of conversion/reconversion reaction. The following charge processes enable the further lowering of charge overpotential compared with the first charge. The electrochemical grinding of LiF domains after the first cycle is responsible for the narrowing of charge polarization and the further enhancement of energy efficiency (76%). After 50 cycles, the discharge capacity is still as high as 404 mAh g^{-1} with a high coulombic efficiency as shown in Fig. 5b. The potential deformation and disconnection of triple-phase catalytic interfaces may be responsible for the gradual capacity attenuation during the early cycles. However the capacity performance and cycling stability are still much better than the solid-solution Ni-Fe-F cathode reported by Huang et al. [22]. Fig. 5c displays the rate capability of NFF thin film at much higher current densities. The reversible capacities as still as high as 435.38, 390.77, 358.46, 329.23 and 306.15 mAh g^{-1} at 769.38, 1154.07, 1538.76, 1923.45 and 3846.9 mA g^{-1} respectively. The following capacity can still recover to 473.84 mAh g^{-1} when the current density returns to 385 mA g^{-1}. Our NFF cathode displays the evident advantages in terms of both the energy and power densities over already reported LiF-driven conversion systems (LiF/M, LiF/MO and LiF/MF_2) as well as ternary fluoride systems (Fig. 5d) [17,22–28,30,49–52]. The energy density of NFF cathode is as high as 1414 Wh kg^{-1} under a high power density of 849 W kg^{-1} and it can still be maintained at 690 and 629 Wh kg^{-1} under the extremely high power densities of 2226 and 3374 W kg^{-1} respectively.

The pseudocapacitance arises from a faradaic-reaction-like process (i.e. electrochemical process that involves chemical changes in electroactive material with faradic charge transfer) at the electrode surface with intercalation, underpotential deposition or redox processes [53]. It is not an electrostatic capacitance like that of the double layer, and the pseudocapacitance can be 10–100 times the double-layer capacitance based on the same electrode area. Its discharge and recharge behavior usually exhibits a high degree of kinetic reversibility. The total stored charge can be separated into three components: the faradaic contribution from the Li^+ ion diffusion process, the faradaic contribution from the charge-transfer process with surface atoms (referred as pseudocapacitance), and the nonfaradaic contribution from the double layer effect. When the particle size of active species is reduced to nanoscale as in this thin film system, the faradaic reaction occurring at the surface atoms (i.e. surface pseudocapacitive effect) would dominate, and correspondingly the diffusion-controlled faradaic process would shrink. In our case, the nonfaradaic contribution from the double layer effect can be ruled out, and therefore the charge storage can be mainly ascribed into two parts: bulk reaction (controlled by faradaic diffusive process) and (near)surface reaction (related to faradaic pseudocapacitance). In Fig. 6, the contributions of faradaic bulk diffusion and surface pseudocapacitance are distinguished from the CV experiment under various scan rates (ν) from 0.1 to 1.0 mV s^{-1}. The logarithm of peak current (i_p) presents a nearly linear relationship with the logarithm of scan rate (ν) in Fig. 6b, which can be expressed according to the following equation [54]:

$$i_p = a\nu^b \text{ or } \ln i_p = \ln a + b\ln\nu$$

where a and b are the adjustable parameters. The electrochemical reaction is dominated by capacitance process when b is close to 1, whereas it is diffusion-controlled with faradaic process when b approaches to 0.5 [54]. The cathodic peak C_2 referring to the main reduction of Fe/Ni cations to metallic Fe^0/Ni^0 has a high fraction of faradaic diffusion contribution because of b = 0.54. The b values for other redox peaks exceed 0.8, indicating a dominant contribution of pseudocapacitance effect, which even dominates the catalytic LiF splitting steps. The total current response can be quantitatively distinguished into the faradaic capacitive and diffusive contributions ($k_1\nu$ and $k_2\nu^{1/2}$, respectively) according to the following equation [54]:

$$i_p = k_1\nu + k_2\nu^{1/2} \text{ or } i_p/\nu^{1/2} = k_1\nu^{1/2} + k_2$$

As demonstrated in Fig. 6c, the corresponding capacitive current as a function of potential could be obtained by calculating the $k_1\nu$ value. The percent of capacitive charge exceeds 50% in the whole electrochemical window under various scan rate conditions and it is as high as 68% at 1 mV s^{-1} (Fig. 6d). This fraction is lower than that of already reported LiF-MO systems (with 94% capacitive charge) [26], indicating that a sufficient mass diffusion and charge transfer is required to activate the F transport from LiF to metal domains with multiple electron reaction in our NFF system. The percentage of capacitive contribution for most of the redox peaks exceeds 70% as listed in Fig. 6e (apart from the dominant reduction peak C_2, 64%), consisting with the high b value.

The galvanostatic intermittent titration technique (GITT) was conducted to evaluate the Li^+ diffusivity and overpotential performance in NFF thin film during the first cycle (Fig. 7). The overpotential is the difference between the cutoff voltage and open-circuit voltage after relaxation. The overpotential values are roughly stable with less fluctuation during the whole cycling. It is smaller for the catalytic Li splitting process during charging. The GITT measurement was performed at a pulse current of 2 μA cm^{-2} for a duration time of 0.5 h, followed by a relaxation process of 2.5 h (Fig. 7b). After reaching to the quasi-equilibrium potential, the cationic diffusion coefficient (D) could be estimated according to the following simplified equation in view of the linear relationship between transient potential (E) and the square root of intermittent time ($\tau^{1/2}$) (Fig. 7c) [55]:

$$D = \frac{4}{\pi\tau}\left(\frac{m_b V_m}{M_b S}\right)^2\left(\frac{\Delta E_s}{\Delta E_t}\right)^2$$

where m_b, M_b and V_m are the mass, molecular weight and molar volume

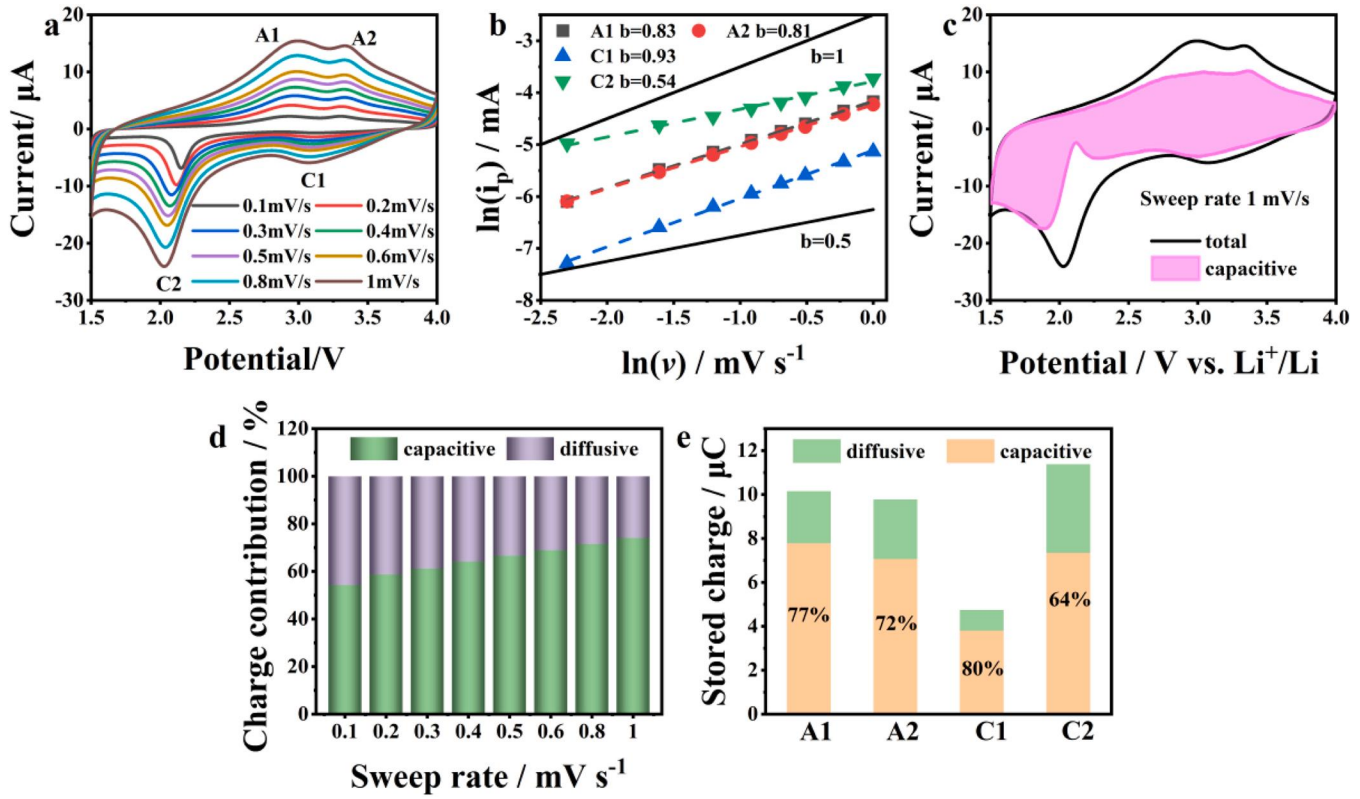

Fig. 6. (a) CV profiles for NFF cathode at various scan rates from 0.1 to 1.0 mV s^{-1} after the first charge. The cathodic and anodic peaks are labeled with A1, A2, C1 and C2. (b) Log-scale plots of peak current versus scan rate and their linear fitting at the corresponding characteristic peak potentials. (c) Overall current response (solid line) and capacitive current profile (shaded region) at the scan rate of 1 mV s^{-1}. (d) Column graphs of sweep-rate-dependent charge storage contributions from both faradaic capacitive and diffusive processes. (e) Column graphs of peak-position-dependent stored charge and contributions from both capacitive and diffusive processes.

of cathode active material respectively, and S is the electrode area. ΔE_s is the difference between two adjacent quasi-equilibrium potentials before and after one complete titration process, and ΔE_t is the difference between potentials at the beginning and termination of titration step. Note that the fluctuation of D values occurs at the transition stage of redox centers with substantial phase transformation (Fig. 7d). The D values mainly lie between 10^{-13} and 10^{-11} cm^2 s^{-1} in most of the reaction voltages, and they are only slightly lower than those of intercalation based cathode materials (10^{-13} to 10^{-8} cm^2 s^{-1}) [56,57], and much higher than those of many other LiF-splitting cathodes (10^{-16} to 10^{-18} cm^2 s^{-1}) [58].

To examine the valence state and evolution of composition in NFF thin films before and after cycling, X-ray photoelectron spectra (XPS) were performed as shown in Fig. 8. The spectra for pristine thin film confirm the coexistence of LiF (at 685.6 eV in F 1 s), metallic Fe (at 707.2 eV in Fe 2p) and Ni (at 853.1 eV in Ni 2p) composite as expected. After the first charge to 4 V, the metallic Fe is oxidized into Fe^{2+}-F and Fe^{3+}-F moieties appearing at 710.4 and 714.2 eV, respectively [30,50]. Meantime Ni^0 is fluorinated into Ni^{2+}-F at 855.7 eV [22]. These oxidization steps are accompanied by the splitting of LiF as indicated by the negative shifting of F 1 s peak to 685.4 eV [30]. From the overlapped Fe 3p and Li 1 s spectra, this LiF splitting process is also proved by the attenuation of Fe^0 peak (at 53 eV) as well as the positive shifting of the peak from 55.6 eV to 56.1 eV with the conversion from Li-F to Fe-F [59,60]. Note that the potential formation of solid-solution $Ni_xFe_{1-x}F_2$ phase at the charge state cannot be ruled out, and the position of Ni-Fe-F signal is very close to that of Fe-F (e.g. around 56 eV) [22,30,60]. After the following discharge to 1.5 V, all the XPS peaks are highly reversible and return back to the original situations with the regeneration of LiF, Fe^0 and Ni^0, consisting with the highly reversible voltage profiles during cycling.

The X-ray absorption near-edge structure (XANES) spectra were carried out to investigate the chemical states of Fe and Ni elements in Fig. 8e and f. For the Fe K-edge spectra, the absorption curves at the pristine and discharge states almost overlap with each other and the corresponding edge positions are similar. It further indicates the high reversibility of electrochemical conversion reaction, consisting with the statement from XPS results. The K-edge position is located at 7112 eV for the discharged electrode, and it is shifted to 7113.5 eV and 7116.5 eV with the formation of Fe^{2+} and Fe^{3+} species respectively for the charged electrode [61]. For the Ni K-edge spectra, the similar curve profiles and edge positions are also observed for the pristine and discharged electrodes. The K-edge position is shifted from 8333 eV to 8339 eV with the oxidation of Ni to Ni^{2+} species [62]. All these observations are completely in line with the XPS results.

In order to identify the conversion products and their distribution during cycling, the TEM results of cycled NFF electrodes are shown in Fig. 9. Upon charging to 4.0 V, the nanodomains of tetragonal rutile phases (e.g. $Ni_xFe_{1-x}F_2$, FeF_2 and NiF_2 with the same space group of P42/mnm) are electrochemically synthesized according to the HRTEM image and SAED pattern in Fig. 9a and b. Besides, FeF_3 domain is also observed from the HRTEM imaging, agreeing with the results of XPS and XANES with the appearance of Fe^{3+} signal. After discharging to 1.5 V, both the HRTEM and SAED in Fig. 9c and d point to the regeneration of Fe, Ni and LiF nanodomains as the conversion products, which are in line with the pristine sample, illustrating the excellent conversion reversibility of LiF/Ni/Fe system. According to the result of EDS mapping for the charged sample (Fig. 9e), the Fe and Ni elements are not only highly dispersive but also superposed, in view of the potential formation of solid-solution $Ni_xFe_{1-x}F_2$ phase. Note that there are visible

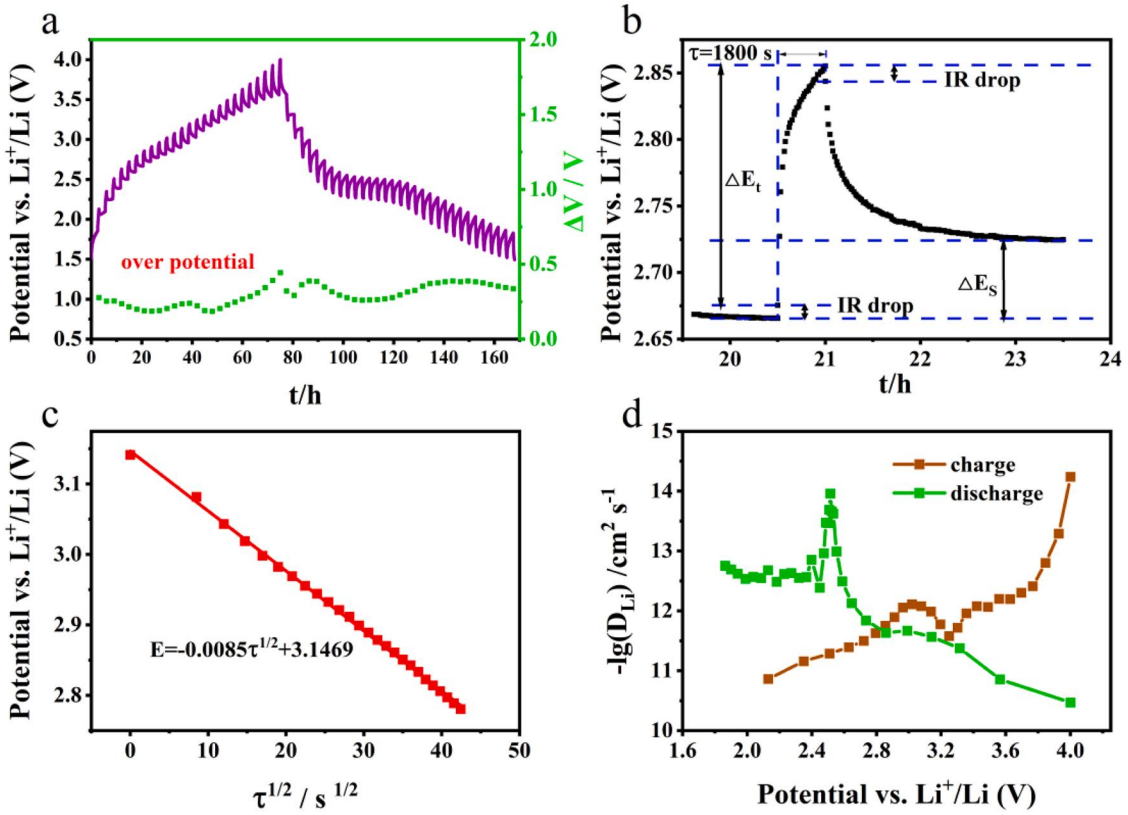

Fig. 7. (a) Potential response and overpotential evolution of NFF thin film during GITT measurement at a pulse current of 2 μA cm^{-2} for a duration of 0.5 h, followed by a relaxation of 2.5 h. (b) Schematic of GITT profile for a whole process and parameter illustration. (c) Linear fitting of transient voltage (E) as a function of the square root of current pulse time ($\tau^{1/2}$). (d) Diffusion coefficient estimated from GITT as a function of reaction potential during discharge and charge processes.

uncolored voids especially in the Ni element mapping, indicating the precipitation of NiF_2 phase around the $Ni_xFe_{1-x}F_2$ domains. This phenomenon is likely responsible for the higher percentage of Ni content than Fe content in the line scan test across the selected region (Fig. 9g). For the discharged region (Fig. 9f), the element segregation of Ni is evidently alleviated in view of the F extraction and volume shrinkage. Therein the metallic Ni and Fe domains have the more consistent spatial distributions in view of their lattice matching. The interconnection of dual metal nanodomains is clearly observed, benefiting to the preservation of built-in conductive network and the following electrochemical cycling. We also note that the F element coloring becomes less continuous, and it is caused by the regeneration of LiF clusters segregated by surrounding metallic nanodomains. The electrochemical grinding of LiF into finer clusters is expected to further promote the interconnectivity of metallic networks. Therefore, from the EDS line scan test, the contents of Ni and Fe become close compared with the situation of charged region. This component percentage distribution is comparable to the pristine situation (before cycling) with the equal percentages of Ni and Fe elements. The analysis of component spatial distribution provides the microstructure proof on the promotion of conversion reaction reversibility.

The reaction mechanism scheme of NFF during the first charge and discharge is shown in Fig. 10. The LiF is first electrochemically splitted with the Li extraction, and simultaneously the left F^- anion is prone to diffuse and bond with the most adjacent Fe and Ni domains after electron extraction. This process is triggered from the LiF-Fe or LiF-Ni interface by F-ion transfer. The compact interface contact in the thin film configuration is favorable for the short-range F-mass transfer, leading to the promotion of LiF splitting kinetics. The charge process enables the formation of $Ni_xFe_{1-x}F_2$, FeF_2 and NiF_2 based on the similar rutile structure. The adjacent distribution of Ni and Fe with tiny nanodomain size guarantees the homogeneous reconversion reaction with the appearance of long charge plateau and formation of solid-solution $Ni_xFe_{1-x}F_2$. Due to the structural similarity between FeF_2 and NiF_2, the nucleation and subsequent growth of Ni-dominant fluoride phase on the pre-formed Fe-fluoride surface likely demands less energy than the direct nucleation of NiF_2 [22]. On the other hand, the residual Ni^0 domains or clusters catalytically promote the Li-F splitting with the supply of more dissociated F^- for the bonding with surrounding Ni cations. Both the factors would remarkably lower the energy barrier and charge voltage for Ni-F bonding (close to the charge voltage of Fe-F bonding, Fig. 2d), and therefore increase the potentiality of Ni-F doping into Fe-F lattices with the formation of $Ni_xFe_{1-x}F_2$ (Fig. 9). Some Fe^{2+}-F/Li-F interfaces can be further electrochemically activated with the formation of FeF_3 at the higher voltage. During the following discharge, the Fe^{3+}-F moieties are prone to be reduced earlier at the higher voltage region. Then the longer discharge plateau is responsible for the deeper reduction of Ni^{2+}-F and Fe^{2+}-F into Ni^0 and Fe^0 with the extraction of F^-, which then bonds with the injected Li^+ to precipitate LiF clusters in metallic network. Note the modification of Ni-F in Fe-F lattices enables the evident enhancement of discharge voltage compared with the undoped Fe-F lattices due to the higher EMF of NiF_2 (Fig. 2d). The precipitation of LiF and metal domains with sufficient mixed conductivity would not retard the later Li diffusion and access to the residual M-F species, guaranteeing the progress of lithiation conversion reaction. The pre-lithiated NFF thin film can be considered as promising cathode in the field of microbatteries or thin film solid state batteries based on Li-free or Li-few anode [63,64]. The high conversion reaction capacity is expected to offer adequate energy for intelligent microsystems. The thin film configuration is designed in order to promote the heterostructure dispersion and contact with better charge/mass transfer capability. However it is still a challenge to extend the NFF heterostructure to the corresponding LiF-contained powder system without performance degradation in view of the phase contact degradation even under the

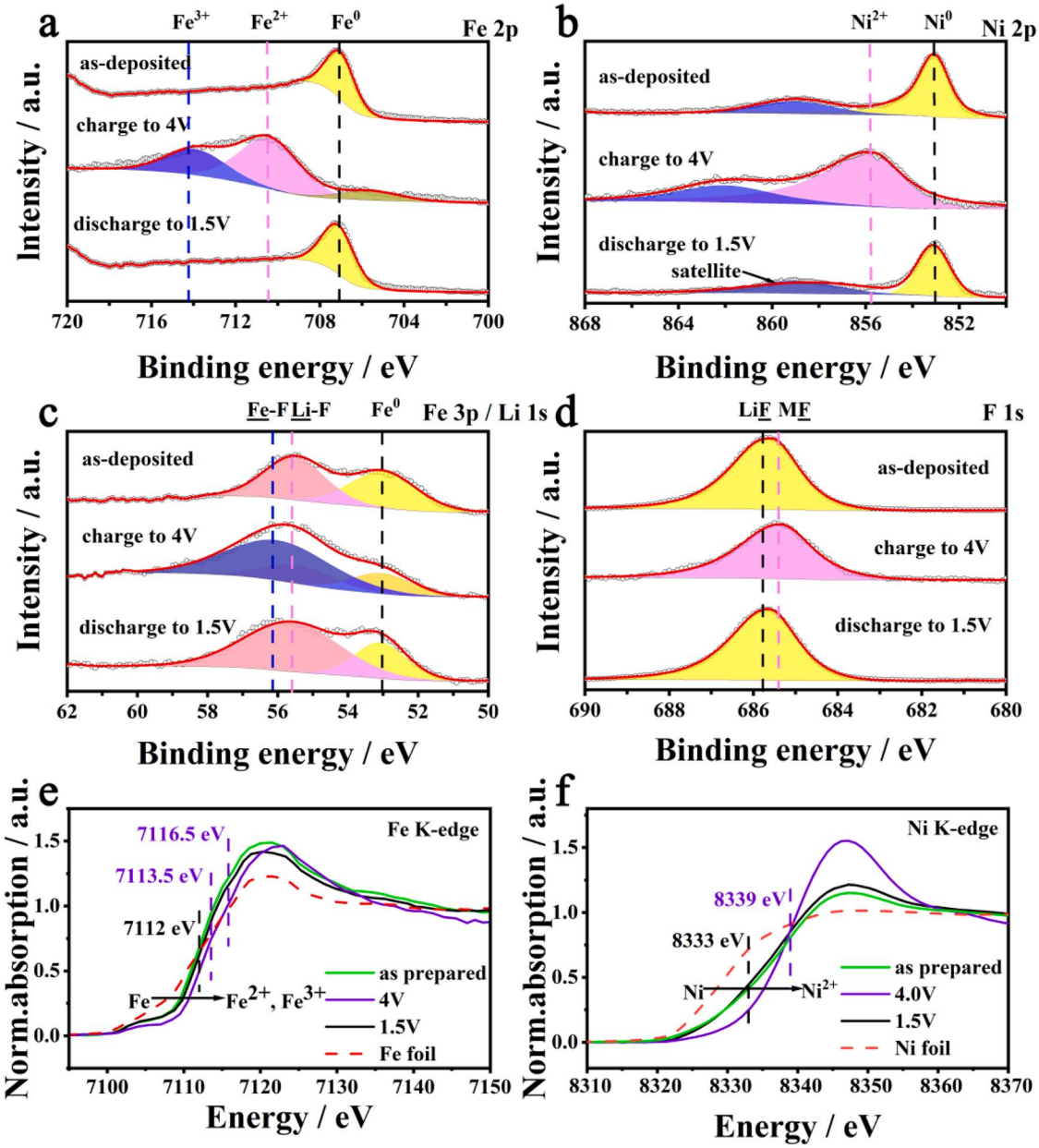

Fig. 8. XPS spectra of (a) Fe 2p, (b) Ni 2p, (c) Fe 3p and Li 1 s, (d) F 1 s for pristine NFF and cycled electrodes after charge to 4 V and discharge to 1.5 V. Normalized (e) Fe K-edge and (f) Ni K-edge XANES spectra of Fe foil, Ni foil, pristine NFF, and cycled electrodes after charge to 4 V and discharge to 1.5 V.

nanodomain scale. More efforts are required to stabilize the conversion reaction, mitigate the phase segregation and dead-zone formation during long-term cycling.

3. Conclusion

In summary, a dual-metal induced acceleration of LiF splitting is proposed to achieve a lithiated ternary fluoride cathode (LiF/Ni/Fe) with superior conversion reaction capacity and rate performance. The crowded effect of multiphases suppresses the growth of crystal grains and promotes the enrichment and penetration of LiF-metal interfaces. The DFT calculations demonstrate the catalysis effect of metallic Ni on lowering the dissociation energy of LiF and charge overpotential. The sufficient triple-phase interface contact and interconnectivity of electron conductive network endow the lithiated fluoride with an ultrahigh initial charge capacity exceeding 600 mAh g^{-1} and lowered charge plateau below 3.5 V. The following discharge capacity is as high as 600 mAh g^{-1} and still preserved at 500 and 400 mAh g^{-1} after 10 and 50 cycles respectively. The electrochemical synthesis of rutile-like $Ni_xFe_{1-x}F_2$ solid-solution phase is responsible for the achievement of high energy efficiency of 76%. This fluoride cathode enables a delivering of high energy density (1414 Wh kg^{-1}) under a power density of 849 W kg^{-1} and the energy density can be maintained at 629 Wh kg^{-1} under an extremely high power densities of 3374 W kg^{-1}.

CRediT authorship contribution statement

Tao Wu: Investigation, Formal analysis, Methodology, Writing – original draft. **Yanhua Cui:** Supervision, Conceptualization, Methodology, Writing – review & editing. **Kaiyuan Wei:** Investigation. **Chuanzhong Lai:** Formal analysis, Writing – original draft. **Yu Zhao:** Investigation. **Shuang Ni:** Investigation. **Yongjin Chen:** Investigation. **Xiang Gao:** Investigation. **Yixiu Cui:** Supervision. **Chilin Li:** Conceptualization, Methodology, Supervision, Writing - original draft, Writing -

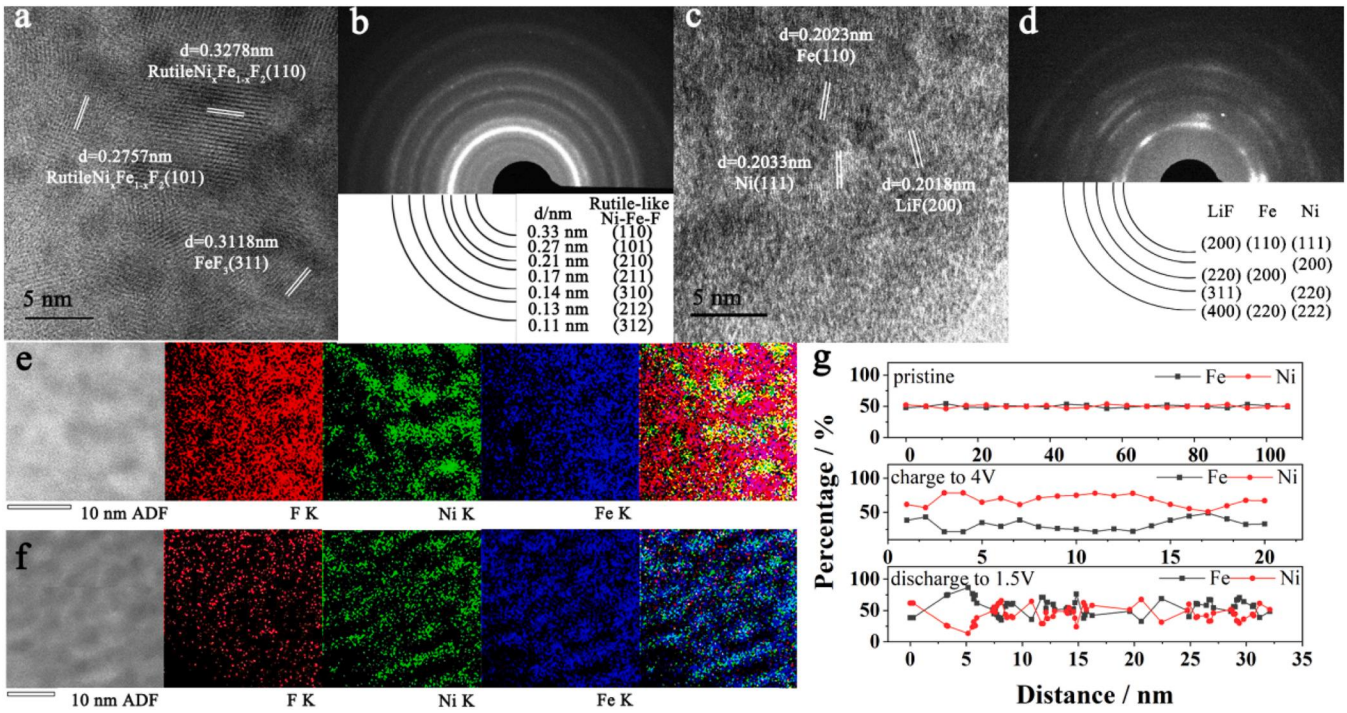

Fig. 9. HRTEM images of cycled NFF electrodes after (a) charge to 4 V and (c) discharge to 1.5 V, and their corresponding SAED patterns in (b) and (d), respectively. EDS elemental mapping of NFF electrodes after (e) charge to 4 V and (f) discharge to 1.5 V by spherical aberration electron microscopy method. (g) EDS line scan results to disclose the distribution of Ni and Fe contents in selected region for pristine and cycled electrodes.

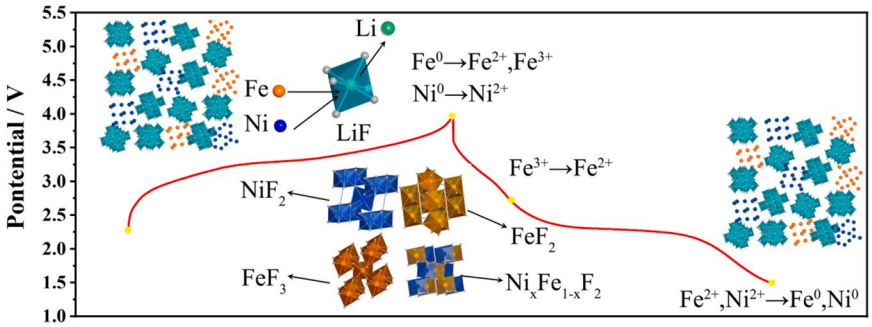

Fig. 10. Schematic illustration of conversion reaction mechanism for NFF thin film electrode during the first charge and discharge.

review & editing.

Declaration of Competing Interest

The authors declare that they have no known competing financial interests or personal relationships that could have appeared to influence the work reported in this paper.

Data Availability

Data will be made available on request.

Acknowledgements

This work was financially supported by NSAF (Grant No. U1930208), National Natural Science Foundation of China, (Grant No. 21975276, 22102163), CAEP foundation (Grant No. CX20200009), the State Key Laboratory of Physical Chemistry of Solid Surfaces of Xiamen University (Grant No. 2020Z01) and Shanghai Science and Technology Committee (Grant No. 20520710800, 21XD1424400). The authors acknowledge the Hard X-ray Microfocus Beamline BL15U1 of the Shanghai Synchrotron Radiation Facility.

Appendix A. Supporting information

Supplementary data associated with this article can be found in the online version at doi:10.1016/j.nanoen.2022.107843.

References

[1] M. Armand, J.M. Tarascon, Nature 451 (2008) 652–657.
[2] V. Etacheri, R. Marom, R. Elazari, G. Salitra, D. Aurbach, Energy Environ. Sci. 4 (2011) 3243–3262.
[3] F. Wu, G. Yushin, Energy Environ. Sci. 10 (2017) 435–459.
[4] J. Hu, Y. Zhang, D. Cao, C. Li, J. Mater. Chem. A 4 (2016) 16166–16174.
[5] A.W. Xiao, H.J. Lee, I. Capone, A. Robertson, T.U. Wi, J. Fawdon, S. Wheeler, H. W. Lee, N. Grobert, M. Pasta, Nat. Mater. 19 (2020) 644–654.
[6] K. Chen, M. Lei, Z. Yao, Y. Zheng, J. Hu, C. Lai, C. Li, Sci. Adv. 7 (2021) eabj1491.
[7] C. Li, K. Chen, X. Zhou, J. Maier, npj Comput. Mater. 4 (2018) 22.
[8] W. Gu, O. Borodin, B. Zdyrko, H.-T. Lin, H. Kim, N. Nitta, J. Huang, A. Magasinski, Z. Milicev, G. Berdichevsky, G. Yushin, Adv. Funct. Mater. 26 (2016) 1507–1516.
[9] L. Li, F. Meng, S. Jin, Nano Lett. 12 (2012) 6030–6037.
[10] M. Sina, R. Thorpe, S. Rangan, N. Pereira, R.A. Bartynski, G.G. Amatucci, F. Cosandey, J. Phys. Chem. C 119 (2015) 9762–9773.

[11] X. Hua, R. Robert, L.-S. Du, K.M. Wiaderek, M. Leskes, K.W. Chapman, P.J. Chupas, C.P. Grey, J. Phys. Chem. C 118 (2014) 15169–15184.
[12] F. Badway, F. Cosandey, N. Pereira, G.G. Amatucci, J. Electrochem. Soc. 150 (2003) A1318–A1327.
[13] C. Li, C. Yin, L. Gu, R.E. Dinnebier, X. Mu, P.A. van Aken, J. Maier, J. Am. Chem. Soc. 135 (2013) 11425–11428.
[14] D. Gordon, Q. Huang, A. Magasinski, A. Ramanujapuram, N. Bensalah, G. Yushin, Adv. Energy Mater. 8 (2018), 1800213.
[15] D. Cao, C. Yin, J. Zhang, C. Li, Chin. Sci. Bull. 62 (2017) 897–907.
[16] F. Badway, N. Pereira, F. Cosandey, G.G. Amatucci, J. Electrochem. Soc. 150 (2003) A1209–A1218.
[17] F. Wang, S.-W. Kim, D.-H. Seo, K. Kang, L. Wang, D. Su, J.J. Vajo, J. Wang, J. Graetz, Nat. Commun. 6 (2015) 6668.
[18] C. Li, X. Mu, P.A. van Aken, J. Maier, Adv. Energy Mater. 3 (2013) 113–119.
[19] W. Li, Y. Chen, A. Zangiabadi, Z. Li, X. Xiao, W. Huang, Q. Cheng, S. Lou, H. Zhang, A. Cao, X. Roy, Y. Yang, ACS Appl. Mater. Interfaces 12 (2020) 33803–33809.
[20] F. Wang, R. Robert, N.A. Chernova, N. Pereira, F. Omenya, F. Badway, X. Hua, M. Ruotolo, R. Zhang, L. Wu, V. Volkov, D. Su, B. Key, M.S. Whittingharn, C. P. Grey, G.G. Amatucci, Y. Zhu, J. Graetz, J. Am. Chem. Soc. 133 (2011) 18828–18836.
[21] Y.T. Teng, F. Wei, R. Yazami, J. Alloy. Compd. 653 (2015) 434–443.
[22] Q. Huang, T.P. Pollard, X. Ren, D. Kim, A. Magasinski, O. Borodin, G. Yushin, Small 15 (2019), 1804670.
[23] X. Fan, Y. Zhu, C. Luo, L. Suo, Y. Lin, T. Gao, K. Xu, C. Wang, ACS Nano 10 (2016) 5567–5577.
[24] G.G. Amatucci, N. Pereira, F. Badway, M. Sina, F. Cosandey, M. Ruotolo, C. Cao, J. Fluor. Chem. 132 (2011) 1086–1094.
[25] S.-W. Kim, K.-W. Nam, D.-H. Seo, J. Hong, H. Kim, H. Gwon, K. Kang, Nano Today 7 (2012) 168–173.
[26] S.-K. Jung, H. Kim, M.G. Cho, S.-P. Cho, B. Lee, H. Kim, Y.-U. Park, J. Hong, K.-Y. Park, G. Yoon, W.M. Seong, Y. Cho, M.H. Oh, H. Kim, H. Gwon, I. Hwang, T. Hyeon, W.-S. Yoon, K. Kang, Nat. Energy 2 (2017) 16208.
[27] R. Prakash, A.K. Mishra, A. Roth, C. Kuebel, T. Scherer, M. Ghafari, H. Hahn, M. Fichtner, J. Mater. Chem. 20 (2010) 1871–1876.
[28] X. Fan, Y. Zhu, C. Luo, T. Gao, L. Suo, S.-C. Liou, K. Xu, C. Wang, J. Power Sources 307 (2016) 435–442.
[29] R. Prakash, C. Wall, A.K. Mishra, C. Kuebel, M. Ghafari, H. Hahn, M. Fichtner, J. Power Sources 196 (2011) 5936–5944.
[30] Y. Zhao, K. Wei, H. Wu, S. Ma, J. Li, Y. Cui, Z. Dong, Y. Cui, C. Li, ACS Nano 13 (2019) 2490–2500.
[31] K. Wei, Y. Zhao, K. Chen, K. Sun, T. Wu, Z. Dong, Y. Cui, C. Zeng, C. Li, Adv. Funct. Mater. 31 (2021), 2009133.
[32] C.L. Li, L. Gu, X.X. Guo, D. Samuelis, K. Tang, J. Maier, Nano Lett. 12 (2012) 1241–1246.
[33] P. Briois, M. Arab-Pour-Yazdi, N. Martin, A. Billard, Coatings 10 (2020) 224.
[34] C.L. Li, X.X. Guo, L. Gu, D. Samuelis, J. Maier, Adv. Funct. Mater. 21 (2011) 2901–2905.
[35] W.J. Qiu, Z.S. Li, K.Y. Chen, C.L. Li, J.J. Liu, W.Q. Zhang, ACS Appl. Mater. Interfaces 11 (2019) 37768–37778.
[36] P. Yu, C. Li, X. Guo, J. Phys. Chem. C 118 (2014) 10616–10624.
[37] H. Li, P. Balaya, J. Maier, J. Electrochem. Soc. 151 (2004) A1878–A1885.
[38] Y. Sun, H.-W. Lee, G. Zheng, Z.W. Seh, J. Sun, Y. Li, Y. Cui, Nano Lett. 16 (2016) 1497–1501.
[39] H. Yang, Y. Li, D. Wu, Z.-R. Li, Inter. J. Quantum Chem. 112 (2012) 770–778.
[40] Z. Yang, S. Zhao, Y. Pan, X. Wang, H. Liu, Q. Wang, Z. Zhang, B. Deng, C. Guo, X. Shi, ACS Appl. Mater. Interfaces 10 (2018) 3142–3151.
[41] Y. Xu, A.V. Ruban, M. Mavrikakis, J. Am. Chem. Soc. 126 (2004) 4717–4725.
[42] Z. Rong, D. Kitchaev, P. Canepa, W. Huang, G. Ceder, J. Chem. Phys. 145 (2016), 074112.
[43] S. Shi, Y. Qi, H. Li, L.G. Hector, J. Phys. Chem. C 117 (2013) 8579–8593.
[44] R.R. Li, H.J. Peng, Q.P. Wu, X.J. Zhou, J. He, H.J. Shen, M.H. Yang, C.L. Li, Angew. Chem. Int. Ed. 59 (2020) 12129–12138.
[45] Q.P. Wu, Z.G. Yao, X.J. Zhou, J. Xu, F.H. Cao, C.L. Li, ACS Nano 14 (2020) 3365–3377.
[46] J. Tafel, Z. Phys. Chem. 50 (1905) 641–712.
[47] K.Y. Chen, W.J. Qiu, Q.P. Wu, X.J. Zhou, J.J. Liu, C.L. Li, J. Mater. Chem. A 9 (2021) 6160–6171.
[48] P.L. Allen, A. Hickling, Trans. Faraday Soc. 53 (1957) 1626–1635.
[49] Y. Tomita, H. Nasu, Y. Izumi, J. Arai, S. Otsuka, Y. Yamane, K. Yamada, Y. Kohno, K. Kobayashi, J. Power Sources 329 (2016) 406–411.
[50] L. Liu, M. Zhou, L. Yi, H. Guo, J. Tan, H. Shu, X. Yang, Z. Yang, X. Wang, J. Mater. Chem. 22 (2012) 17539–17550.
[51] Y. Tomita, N. Kimura, Y. Izumi, J. Arai, Y. Kohno, K. Kobayashi, J. Power Sources 354 (2017) 34–40.
[52] A. Kitajou, E. Kobayashi, S. Okada, Electrochemistry 83 (2015) 885–888.
[53] B.E. Conway, J. Electrochem. Soc. 138 (1991) 1539–1548.
[54] J. Tian, X.J. Zhou, Q.P. Wu, C.L. Li, Energy Storage Mater. 22 (2019) 218–227.
[55] K.Y. Chen, Y. Zhang, C.L. Li, ACS Nano 12 (2018) 12444–12455.
[56] H. Xia, L. Lu, G. Ceder, J. Power Sources 159 (2006) 1422–1427.
[57] R. Fallahzadeh, N. Farhadian, Solid State Ion. 280 (2015) 10–17.
[58] J.K. Ko, K.M. Wiaderek, N. Pereira, T.L. Kinnibrugh, J.R. Kim, P.J. Chupas, K. W. Chapman, G.G. Amatucci, ACS Appl. Mater. Interfaces 6 (2014) 10858–10869.
[59] P. Mills, J.L. Sullivan, J. Phys. D 16 (1983) 723–732.
[60] M.U. Kasrai, D.S. Urch, J. Chem. Soc. Faraday Trans. 75 (1979) 1522.
[61] A. Deb, U. Bergmann, E.J. Cairns, S.P. Cramer, J. Phys. Chem. B 108 (2004) 7046–7049.
[62] D.H. Lee, K.J. Carroll, K.W. Chapman, O.J. Borkiewicz, S. Calvin, E.E. Fullerton, Y. S. Meng, Phys. Chem. Chem. Phys. 16 (2014) 3095–3102.
[63] C.L. Li, Z.W. Fu, Electrochim. Acta 52 (2007) 6155–6164.
[64] C.L. Li, B. Zhang, Z.W. Fu, Thin Solid Films 515 (2006) 1886–1892.

Tao Wu received his bachelor's degree from Lanzhou University in 2019. Now he is pursuing his master's degree under the supervision of Prof. Yanhua Cui in the Institute of Electronic Engineering in China Academy of Engineering Physics (CAEP). His research interest focuses on the thin film positive electrodes for thin film Li-ion batteries.

Yanhua Cui is a professor and the leader of the Novel Energy Storage Material group in the Institute of Electronic Engineering, CAEP. She received her bachelor's and master's degrees from the Harbin Engineering University and Ph.D. from Graduate School of CAEP. Her research focuses on the design and application of functional materials for energy storage and conversion.

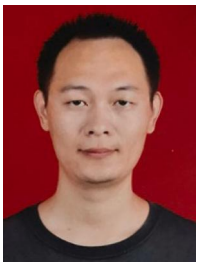

Kaiyuan Wei received his master's degree from China University of Mining and Technology (CUMT) in 2018. He is currently a Ph.D. candidate in the Institute of Electronic Engineering in China Academy of Engineering Physics (CAEP) supervised by Prof. Yanhua Cui. His research interests focus on the thin film Li-ion batteries.

Chuanzhong Lai received his bachelor degree in College of Materials Science and Engineering at Sichuan University. He is currently a Ph.D. candidate in the Shanghai Institute of Ceramics, Chinese Academy of Sciences under the supervision of Prof. Chilin Li. His major interest focuses on the research and development of high-capacity cathode materials for Li-ion and Li-metal batteries.

Yu Zhao received his M.E. from University of Science and Technology of China in 2015. Now he is pursuing his Ph.D. at Graduate School of China Academy of Engineering Physics. His current research interest focuses on the thin film Li-ion batteries.

Shuang Ni received his doctor's degree from University of Science and Technology of China in 2015. His current research interest focuses on the detection of virus using Raman spectra.

Yongjin Chen is currently a staff scientist in the Center for High Pressure Science & Technology Advanced Research (HPSTAR). He obtained his bachelor degree from Sichuan University, and completed his Ph.D. in Physics from Beijing University of Technology in 2019. He then worked as a post-doctoral research fellow at HPSTAR Beijing (2019–2021). His research interests focus on the advanced transmission electron microscopy techniques, energy related materials and phase change memory materials.

Xiang Gao received his Ph.D. in 2011 from the Shanghai Institute of Ceramics, Chinese Academy of Sciences. He became a principal investigator at the Center for High Pressure Science and Technology Advanced Research (HPSTAR) in 2018. His research interests focus on the microstructure sciences and engineering of advanced functional materials.

Yixiu Cui is a professor in the Institute of Electronic Engineering, CAEP. She received her master's degree from University of Electronic Science and Technology of China. Her research focuses on the engineering development of special power supply.

Chilin Li received his Ph.D. degree in 2008 at Fudan University. He is now a professor in Shanghai Institute of Ceramics, Chinese Academy of Sciences (SICCAS). His research interest focuses on fluoride-based batteries, solid-state batteries, Li and Mg metal batteries, structure design and synthesis strategy of novel electrode and electrolyte materials, electrochemical mechanism, nanoionics.